DOI: 10.12442/j.issn.1002-185X.20250488

From Withdrawal Rate to Creep Life: Microstructure-Mediated Performance in Directionally Solidified Mar-M247LC

Gan Yisheng [a,1], Wang Haiyang [b,c,1*], Zhong Hong [a*], Zhu Jiaxi [a], Li Bo [a], Feng Zhenyu [a], Li Shuangming [a]

[a] *State Key Laboratory of Solidification Processing, Northwestern Polytechnical University, Xi'an, 710072, P. R. China*

[b] *State Key Laboratory of Clean and Efficient Turbomachinery Power Equipment, Deyang, 618000, China*

[c] *Dongfang Electric Corporation Dongfang Turbine Co., LTD, Deyang, 61800, China*

**Corresponding authors*

State Key Laboratory of Clean and Efficient Turbomachinery Power Equipment, Deyang, 618000,P. R. China

E-mail address: wanghy@dongfang.com (Wang Haiyang).

State Key Laboratory of Solidification Processing,

Northwestern Polytechnical University,

Xi'an, 710072, P. R. China

E-mail address: zhonghong123@nwpu.edu.cn (Zhong Hong).

[1] These authors contribute equally

Rare Metal Materials and Engineering

Abstract

Directionally solidified (DS) nickel-based superalloys exhibit excellent creep resistance due to the elimination of transverse grain boundaries perpendicular to the stress axis. Given the strong dependence of creep performance on the initial solidification microstructure, this study reveals how withdrawal rate governs the as-cast microstructure of DS Mar-M247LC and dictates its post-heat-treatment creep life at 980 °C/220 MPa. It was found that an increase in the withdrawal rate of the directionally solidified specimens led to a reduction in the values of primary dendrite arm spacing (from 479 μm to 322 μm) and the average size of γ' precipitates (from 460 nm to 345 nm in interdendritic regions and from 298 nm to 203 nm in dendritic core). In addition, the carbide morphology changes from blocky to script-like. The heat treatment led to the formation of distinct cuboidal γ' precipitates and was accompanied by a significant increase in the γ' volume fraction compared to the directionally solidified microstructure. The alloy solidified at 40 μm/s exhibits elongated γ' rafts with narrowed matrix channels and regular dislocation networks, synergistically extending creep rupture life to 96.6 h. Fractographic analysis confirmed transgranular ductile, with fracture initiation occurring at decomposed MC carbides.

Keywords: Directionally solidified nickel-based superalloy; Withdrawal rate; Microstructure; Creep

Rare Metal Materials and Engineering

1. Introduction

Nickel-based superalloys are widely employed in hot-section components of gas turbines and aero-engines due to their excellent high-temperature strength and microstructural stability. To achieve superior high-temperature mechanical properties, these superalloys typically exhibit a high degree of alloying. Elements such as Cr, W, Mo, Hf, Ta, Al, and Ti are added to promote multiple strengthening mechanisms, including solid solution strengthening and precipitation strengthening. Among these, the addition of Ta, Ti, and Al is particularly crucial as it significantly promotes the precipitation of the γ' phase. This coherent nanoscale precipitate provides exceptionally effective strengthening for superalloys [1-5]. The volume fraction and size of the γ' phase significantly influence the endurance properties of the alloy: reducing the γ' phase size or increasing its volume fraction (thereby decreasing inter-particle spacing) both markedly enhance the alloy's creep resistance [6, 7]. Mar-M247 is a precipitation-strengthened Ni-Al-Cr-Co-Ta-W-Hf superalloy. Its relatively high Cr and W contents provide solid solution strengthening [8], while the high combined addition of Ta, Ti, and Al (up to 9.5wt%) ensures a substantial γ' phase volume fraction, conferring outstanding creep resistance to this alloy.

At elevated temperatures, the primary manifestation of creep damage in nickel-based superalloys occurs in the form of voids and cavitation nucleation at grain boundaries [3]. Grain boundaries perpendicular to the stress direction often act as crack initiation sites or propagation paths. Directional solidification technology promotes the

Rare Metal Materials and Engineering

growth of columnar grains, effectively eliminating these transverse grain boundaries harmful to creep resistance, thereby significantly enhancing the creep life of superalloys [9, 10]. However, the high concentration of solute elements can lead to segregation during the directional solidification process. Elements with a solidification partition coefficient (k) < 1, such as Nb, Ta, Ti, and Hf, preferentially segregate to the interdendritic regions, causing chemical inhomogeneity [11, 12]. Severe segregation promotes the formation of substantial amounts of γ/γ' eutectic in the interdendritic areas. The presence of γ/γ' eutectic reduces the tensile properties and creep strength of superalloys. Its coarse structure readily acts as a stress concentration point during creep, inducing crack initiation.

Furthermore, in the Mar-M247LC alloy, elements such as Ta, W, and Hf promote the formation of MC carbides. These primary MC carbides are unstable at high temperatures and prone to degenerative decomposition reactions [13, 14]. Qin et al. [15] investigated the influence of primary MC decomposition on the microstructure and endurance properties of nickel-based superalloys, finding that decomposition involves interdiffusion of elements between the primary MC carbides and the γ matrix. This process can, to some extent, increase the γ' phase volume fraction, thereby improving the alloy's endurance properties. Zhang et al. [13], through long-term thermal exposure experiments on directionally solidified nickel-based superalloys, observed that primary MC carbides decompose at grain boundaries, promoting the formation of $M_{23}C_6$ and M_6C carbides. Granular $M_{23}C_6$ carbides can pin dislocations and inhibit grain boundary sliding during deformation [16]. However, when carbides form a continuous chain-like

Rare Metal Materials and Engineering

structure along grain boundaries, they promote grain boundary coarsening, making the boundaries more susceptible to becoming crack initiation sites. Although Mar-M247LC reduces the carbon content to 0.07 wt.% compared to the base Mar-M247 alloy, specifically to mitigate the detrimental effects of carbides on creep properties, elemental segregation inherent to the directional solidification process still leads to the formation of coarse interdendritic MC carbides [8, 17].

Subsequent solution heat treatment processes aim to activate elemental diffusion at high temperatures to promote the dissolution of the eutectic γ' phase and carbides. However, given the low melting point of the eutectic phase, the solution temperature cannot be set too high to avoid incipient melting. Under these constraints, the dissolution of some eutectic increases the saturation level of the matrix. Consequently, this highly saturated matrix cannot dissolve further eutectic, resulting in the retention of a portion of the eutectic within the alloy [2, 18-20]. Therefore, interdendritic segregation and similar inhomogeneities typically cannot be completely eliminated and will still affect the alloy's properties to some extent. Furthermore, merely extending the duration of the solution heat treatment not only reduces production efficiency but also provides limited improvement in solute diffusion. Crucially, prolonged heat treatment can lead to the formation of pores/cavities within the alloy, ultimately degrading its creep life [16, 21-23]. Consequently, compared to relying solely on heat treatment, directly controlling the solidification parameters to manage the initial segregation profile of the alloy proves more effective in enhancing its microstructural homogeneity.

Rare Metal Materials and Engineering

In directional solidification practice, both the temperature gradient (G) and the withdrawal rate (V) are key parameters influencing the microstructure. However, since adjusting the temperature gradient often relies on equipment and is relatively unstable, controlling the withdrawal rate offers a more direct and efficient approach for tailoring the solidification microstructure of superalloys, holding significant importance for optimizing their mechanical properties [9, 24]. Previous studies have demonstrated that increasing the withdrawal rate refines the microstructure. For instance, Li et al. [25] investigated the solidification characteristics and high-temperature tensile properties of IN713C superalloy at different withdrawal rates using directional solidification. They demonstrated that increasing the withdrawal rate promotes the microsegregation of Mo, Nb, and Zr, favoring the precipitation of γ/γ' eutectic and borides. An appropriate increase in withdrawal rate is beneficial for improving high-temperature tensile properties. However, when the withdrawal rate exceeds 50 μm/s, the increased formation of γ/γ' eutectic and borides leads to a decrease in high-temperature strength. Liu et al. [26] studied the effect of withdrawal rate on the segregation behavior of a Ru- and Re-containing nickel-based single-crystal superalloy. They revealed that as the withdrawal rate increases, the degree of segregation of Al, Ta, W, and Re initially increases and then decreases. The reduction in segregation at high withdrawal rates is attributed to the refinement of the dendritic structure. Furthermore, the addition of Ru and Re increases the degree of segregation of Al and Ta.

Therefore, this study systematically examines the influence of withdrawal rate (V = 20–70 μm/s) on the as-cast microstructure of directionally solidified Mar-M247LC

Rare Metal Materials and Engineering

and its subsequent creep performance at 980 °C/220 MPa. The primary focus is to elucidate how *V* governs critical microstructural characteristics—including primary dendrite arm spacing, γ' precipitate size/morphology/volume fraction, and carbide formation—and ultimately dictates the alloy's creep rupture life. A central objective is to identify the optimal *V* that promotes synergistic microstructural features (such as refined γ' rafts, narrowed matrix channels, and regular dislocation networks) for enhanced creep resistance. Additionally, the mechanisms governing creep fracture under these specific conditions are investigated.

2. Experimental

2.1 Sample preparation

The master alloy ingot of nickel-based superalloy Mar-M247LC was used as the raw material, and the nominal composition is listed in **Table 1**. Directionally solidified alloy rods were fabricated via liquid metal cooling (LMC) installation under argon atmosphere with withdrawal rates of 20, 40, and 70 μm/s (named as WR20, WR40, and WR70 in this paper). Subsequently, the DS rods were subjected to a solution heat treatment followed by an aging treatment. The solution treatment consisted of: 1228 °C/2 h+1240 °C/2 h+1255 °C/2 h, air cooling (AC). The aging treatment was: 1079 °C for 4 h, AC; then 870 °C for 20 h, AC. All heat treatments were performed with the rods vacuum-sealed in quartz ampoules.

2.2 Mechanical properties test

Creep rupture tests were conducted on heat-treated Mar-M247LC alloys with

Rare Metal Materials and Engineering

different withdrawal rates under the conditions of 980 °C/220 MPa using an RDL30 creep testing machine. The heat-treated bars were machined into tensile creep specimens having a gauge length of 25 mm and a gauge diameter of 5 mm.

During the test, real-time specimen temperature monitoring was achieved with thermocouples attached at three locations along the gauge length. For each condition, creep tests were performed using two independent samples. All tests were repeated and the results obtained are reproducible.

2.3 Microstructural characterization

Metallographic specimens were sectioned from the DS and Heat-treatment samples. All metallographic specimens were mechanically ground using 400-3000 mesh abrasive paper and polished using 1.5 μm diamond paste. Then, all metallographic specimens were electrolytically etched in a solution of 45vol% H_2SO_4, 42vol% HNO_3, and 13vol% H_3PO_4 at 5V for 3-5s to expose the γ' precipitates, or chemically etched with a solution of 10 ml HNO_3, 20 ml HF, and 30 ml glycerol to expose the γ channel.

Dendritic structures were observed using an Olympus OLS400 laser scanning confocal microscope. General microstructural characterization was performed using a Zeiss Gemini500 scanning electron microscope (SEM). Quantitative microstructural analysis was conducted using the image analysis software Image-Pro Plus 6.0. The area fraction of the γ' phase was measured by image thresholding according to the grey values. To ensure statistical significance, at least three representative images were analyzed for each condition.

Specimens for electron backscattered diffraction (EBSD) analysis were

Rare Metal Materials and Engineering

electropolished for 20 s in a solution of 10vol% perchloric acid in ethanol at 20 V. The phase statistics of the alloy were analyzed on a TESCAN AMBER scanning electron microscopy (SEM) operated at an accelerating voltage of 20 kV, a probe current of 10 nA, and using a scan step size of 0.05 μm.

Dislocation configurations were observed on an FEI Talos F200X transmission electron microscope (TEM) operated at 200 kV. Thin foils for TEM were prepared by punching 3 mm disks, mechanically grinding them to approximately 40 μm thickness, and twin-jet electropolishing in a solution of 10vol% perchloric acid in ethanol at -30 °C and 30 V.

Table 1 The nominal chemical composition (wt%) of Mar-M247LC alloys

Ni	Al	Cr	Co	Ta	W	Hf	Ti	Mo	Zr	C	B
Bal.	5.50	8.00	9.50	3.30	9.40	1.40	0.70	0.50	0.02	0.07	0.016

3. Results and discussion

3.1 Microstructural Evolution in DS Mar-M247LC

3.1.1 Microstructure characterizations

The microstructure of directionally solidified Mar-M247LC alloy undergoes significant evolution with increasing withdrawal rate. Cross-sectional analysis (**Fig. 1a-c**) reveals progressive refinement of the dendritic structure. This dendrite refinement, quantified by a decrease in Primary Dendrite Arm Spacing (PDAS) from 479 ± 22 μm (WR20) to 403 ± 27 μm (WR40) and 322 ± 20 μm (WR70) (**Fig. 1j**), is primarily

Rare Metal Materials and Engineering

governed by increased thermal undercooling and reduced local solidification time at higher withdrawal rates, which restrict dendritic coarsening.

Concurrently, solute segregation dominates interdendritic phase formation. Due to the partition coefficient $k < 1$, γ'-forming elements (Ti, Ta, Al) are rejected into the interdendritic liquid during solidification. This progressively enriches the solutes in the remaining liquid phase, promoting substantial interdendritic eutectic formation.

Phase evolution is further evidenced in γ' precipitates (**Fig. 1d-i**). At alloy WR20, γ' in both dendritic core and interdendritic regions exhibits maximum size and a butterfly morphology. With an incremental withdrawal rate, γ' undergoes progressive refinement and transitions toward a cuboidal shape. Notably, γ' precipitates remain consistently smaller in dendritic cores than in interdendritic regions. Quantitative measurements (**Fig. 1k and l**) confirm these trends: higher withdrawal rates reduce the average γ' diameter while increasing its volume fraction in both regions.

According to the scaling law by Kurz et al. [27], PDAS (λ_1) scales with temperature gradient and cooling rate (R) as:

$$\lambda_1 \propto G^{-0.5} R^{-0.25} \quad (1)$$

In directional solidification with constant G (characteristic of the experimental system), PDAS is dominantly controlled by R. Since cooling rate R correlates linearly with withdrawal rate V ($R = G \times V$), **Eq. (1)** reduces to: $\lambda_1 \propto G^{-0.5} V^{-0.25}$. Experimental data (**Fig. 1j**) confirm this inverse relationship, showing progressive PDAS refinement from 479 ± 22 μm at alloy WR20 to 322 ± 20 μm at alloy WR70 with increasing V.

Carbides in the alloy consistently localize within interdendritic regions across all withdrawal rates, as evidenced in **Fig. 2a-c**. With an incremental withdrawal rate, the carbide morphology evolves markedly: coarse, blocky particles transition to finer,

Rare Metal Materials and Engineering

script-like morphologies with enhanced dispersion. Conversely, quantitative analysis in **Fig. 2d** reveals that withdrawal rate exerts a negligible influence on overall carbide content. **Fig. 2e** and **2f** illustrate the energy dispersive spectroscopy (EDS) point analysis of blocky and rod-like carbides, respectively. The results indicate that Ta is the primary element in these carbides, with Hf and W also present, confirming their classification as MC-type carbides. Additionally, compared to the rod-like carbides, the blocky carbides have a lower Ta content and a significantly higher Hf content.

Although C is added at low levels as an interstitial solute, its pronounced segregation tendency—driven by a low solidification partition coefficient (~0.21)—exceeds that of other alloying elements. This preferential segregation promotes MC carbide formation in interdendritic regions during solidification. At higher withdrawal rates, denser dendritic arrangements restrict carbide growth space, while accelerated cooling suppresses carbide coarsening during subsequent solid-state cooling. These combined effects explain the refined carbide distribution observed at alloy WR70, showing a characteristic of finer, script-like morphology with enhanced dispersion [28].

Rare Metal Materials and Engineering

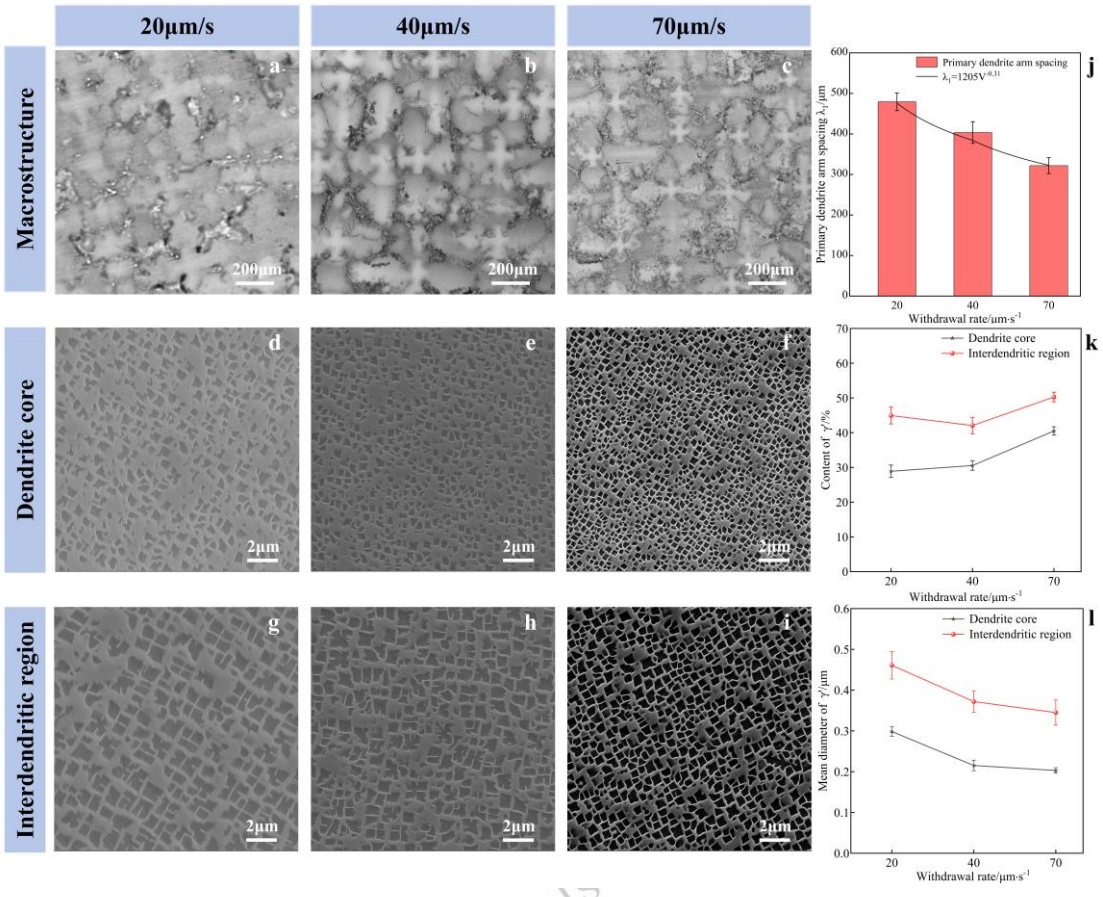

Fig. 1 Microstructural evolution of directionally solidified Mar-M247LC with different withdrawal rates. (a-c) dendritic morphology, (d-f) γ' phase morphology in dendrite core, (g-i) γ' phase morphology in interdendritic region, (j-l) statistical analysis of PDAS, γ' size, and γ' volume fraction.

Rare Metal Materials

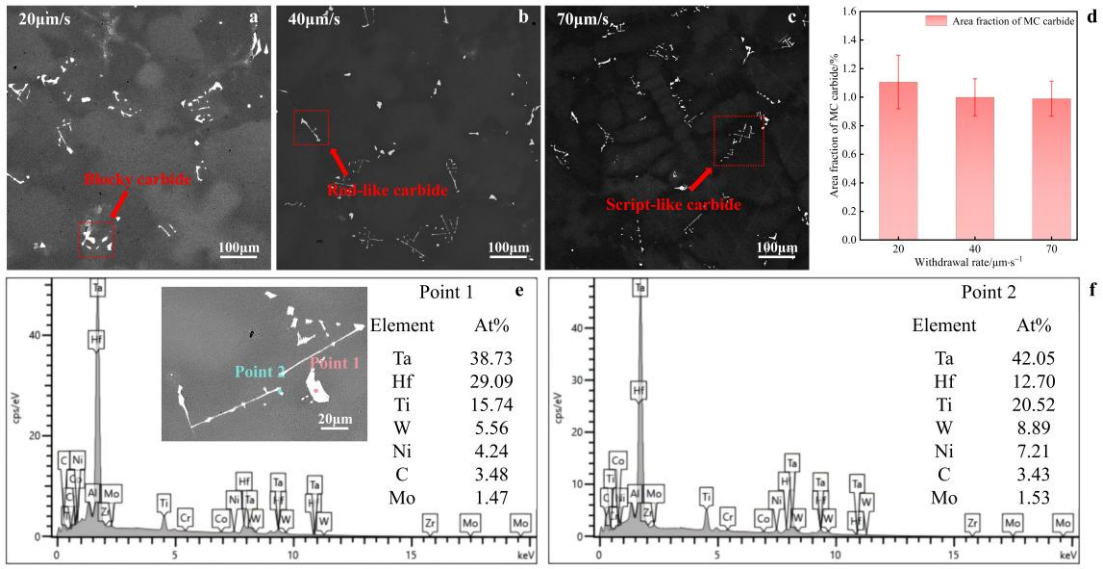

Fig. 2 The differentiation of carbide distribution characteristics with varying withdrawal rate. (a-c) SEM images of microstructural characteristics in WR20, WR40, and WR70 alloys showing the morphology transition from blocky (alloy WR20) to script-like (alloy WR70). (d) Quantitative analysis of carbide content. EDS point analysis results of (e) blocky carbide and (f) rod-like carbide.

3.1.2 Carbide evolution and γ' coarsening in heat-treated state

Representative scanning electron microscopy-backscattered electron (SEM-BSE) images in **Figs. 3** and **4** illustrate the microstructural changes that occur following heat treatment. Compared to the directionally solidified specimens, carbides in the heat-treated samples (**Fig. 3a-c**) exhibit significant refinement and more uniform distribution. Notably, rod-like and script-like carbides decomposed into smaller blocks or fine granular particles. Quantitative analysis revealed a substantial decrease in carbide content (from 0.99% to 0.67%) in the alloy WR70. However, no significant reduction in carbide content was observed in the WR20 (from 1.11% to 1.25%) and WR40 alloys (from 1.0% to 0.88%). **Fig. 3d** illustrates the EDS point analysis of the primary carbides and the granular carbides that precipitated after heat treatment. The results indicate that Hf becomes the dominant element in both types of carbides. Notably, the primary carbides show a significant increase in Hf content, along with a decrease in Ta and Ti concentrations compared to their state in the directionally solidified specimen. This change in composition suggests that the TaC and TiC components in the primary carbides dissolved during heat treatment, allowing Ta and Ti atoms to diffuse into the γ matrix and resulting in the enrichment of Hf.

Rare Metal Materials and Engineering

The preferred order of formation for MC carbides, based on their stability, is HfC, TaC, NbC, and TiC, listed in order of decreasing stability. Blocky MC carbides, which are enriched with Hf compared to their rod-like and script-like counterparts, demonstrate superior thermal stability. This is due to the higher resistance to decomposition of HfC when compared with TaC at elevated temperatures [29]. In contrast to other alloys that contain a significant amount of blocky carbides, the WR70 alloy mainly features rod-like and script-like carbides. During the heat treatment process, these rod-like and script-like carbides undergo substantial decomposition, while the blocky carbides experience much less breakdown.

MC carbides decompose at elevated temperatures, releasing elements (C, Ti, Ta, W, Mo) into the matrix. Crucially, the decomposition of Ta-rich script-like MC carbides elevates the alloy's overall Ta content. This elevated Ta content thermodynamically stabilizes the γ' phase, increasing its equilibrium volume fraction and coarsening rate [29, 30].

The observed carbide evolution directly influences γ' phase development. Higher-magnification views (**Fig. 4a-c**) confirm that the γ' phase developed a uniform distribution and regular cuboidal morphology post-treatment across all samples. Critically, the extent of MC carbide decomposition—and thus Ta release—was significantly greater in the alloy WR70 than in others. Consequently, this alloy exhibited the most pronounced increase in both γ' phase volume fraction and size with increasing withdrawal rate, as quantified in **Fig. 4d-f**.

Rare Metal Materials and Engineering

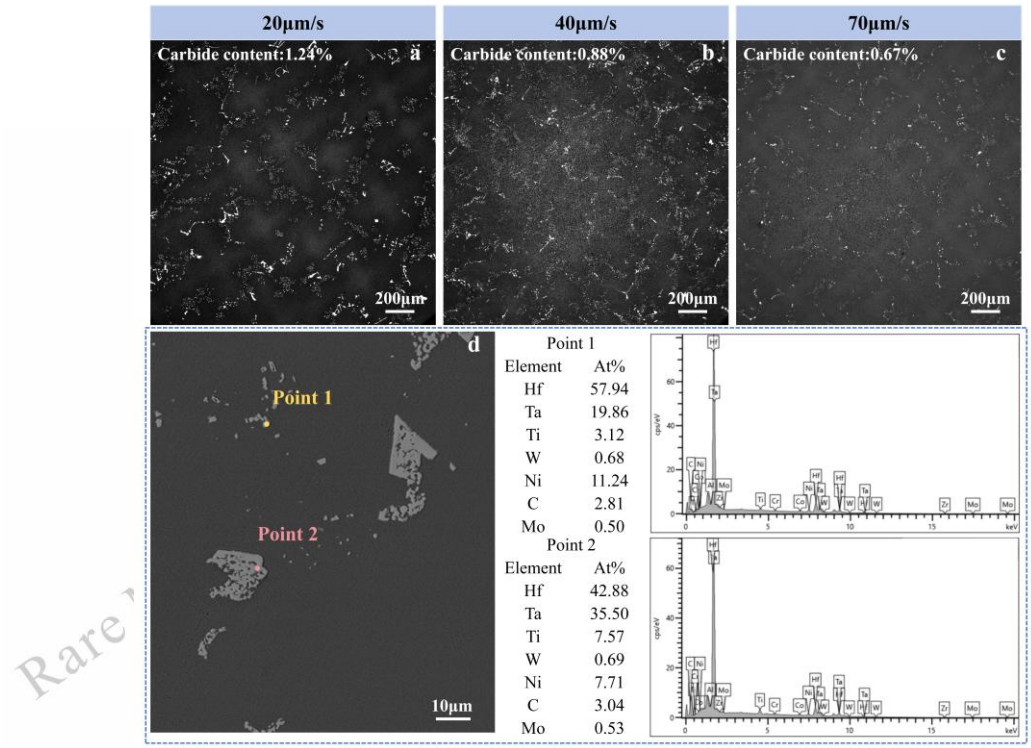

Fig. 3 Evolution of carbide morphology (a-c) and composition (d) in Mar-M247LC superalloy during heat treatment.

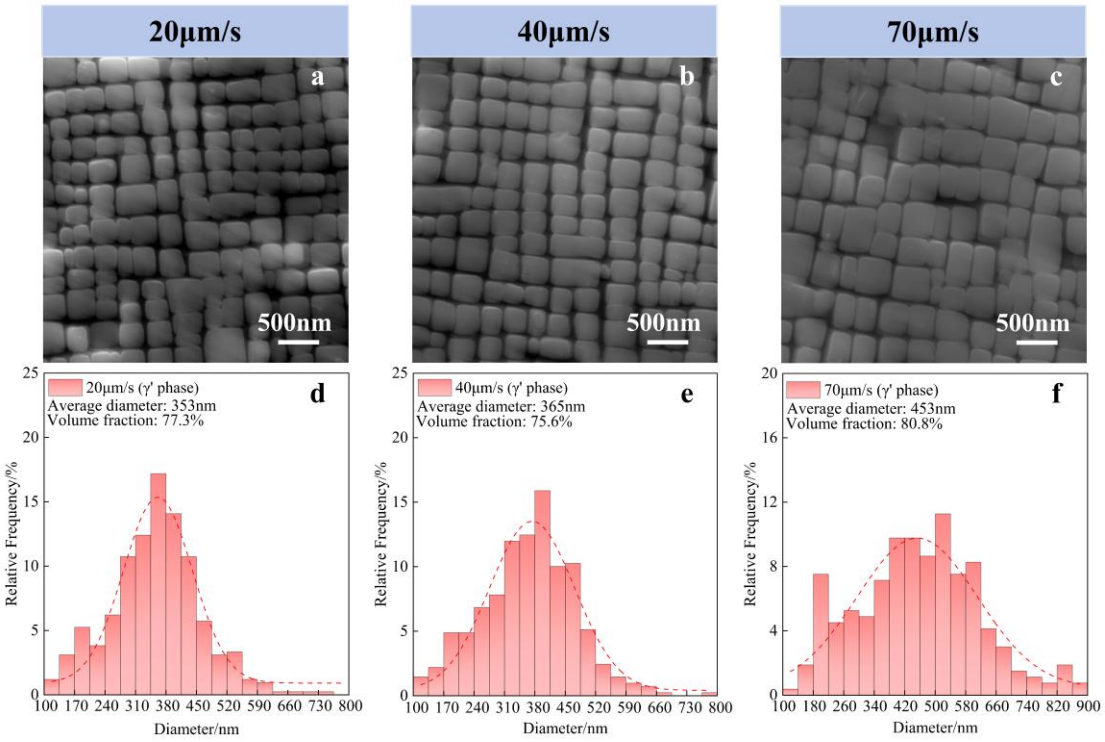

Fig. 4 Analysis of microstructure (a-c), size, and volume fraction (d-f) of γ' precipitates

in Mar-M247LC superalloy after heat treatment.

3.2 Withdrawal rate-dependent creep behavior

Fig. 5 presents the creep rupture curves of different samples under conditions of 980 °C/220 MPa. The alloys solidified at 20, 40, and 70 μm/s exhibit rupture lives of 77.4 h, 96.6 h, and 61.3 h, respectively. With increasing withdrawal rate, the creep rupture life of the specimens first increases and then decreases, indicating that the creep rupture performance exhibits an optimal value with respect to the withdrawal rate.

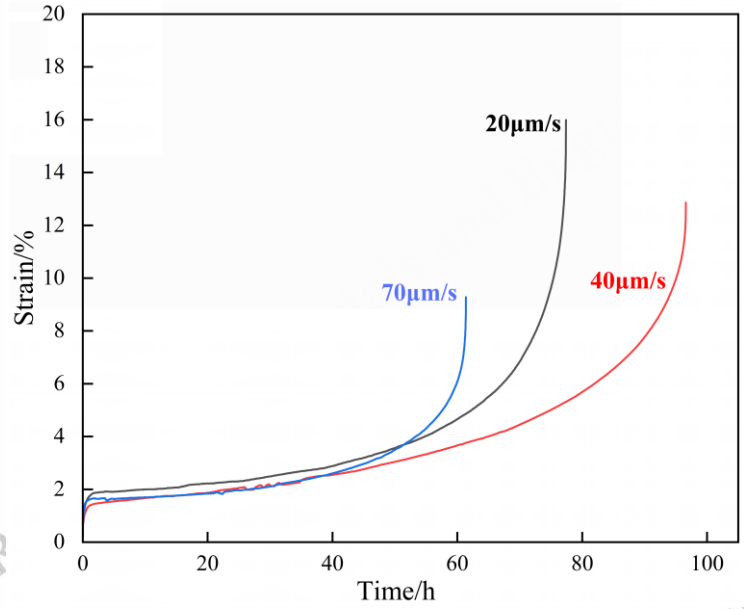

Fig. 5 Creep rupture curves of Mar-M247LC superalloy with varied withdrawal rates at 980 °C/220 MPa.

To investigate the underlying mechanisms of creep behavior, we conducted a meticulous examination of the fractured specimens. The morphologies of the γ' phase near the fracture surface are illustrated in **Fig. 6a-c**. All alloys develop N-type rafted structures perpendicular to the stress axis. In addition, the post-creep γ' rafting morphology adjacent to fracture surfaces shows rate-dependent characteristics.

Compared to the other two alloys, alloy WR40 exhibited narrower (557 nm width) and more elongated γ matrix channels. In contrast, the γ matrix channels in the alloy WR70 showed significant coarsening (676 nm width).

During creep deformation, the γ' phase coalesces and merges under the applied stress, forming an elongated rafted structure [30]. Under high-temperature and low-stress testing conditions, creep deformation is governed by the movement and climbing of dislocations within the γ matrix for alloys strengthened by a high volume fraction of the γ' phase. The formation of rafted structures significantly increases the distance dislocations must climb, thereby enhancing the creep resistance [31, 32]. Smaller γ' precipitates result in narrower γ matrix channels after rafting. These narrower channels hinder dislocation movement within the γ matrix channels. Furthermore, the constricted γ matrix channels make it considerably more difficult for dislocations to bypass the γ' precipitates via climb; instead, they are forced to shear through the γ' phase [33-36]. Consequently, the alloy WR40, characterized by longer rafts and narrower γ matrix channels, exhibits superior resistance to dislocation motion compared to the alloys solidified at other withdrawal rates. This results in its higher creep rupture life. Conversely, the deviation in the orientation of the rafted structures in alloys WR20 and WR70 specimens reduces their effectiveness in impeding dislocation movement, leading to their lower creep lives compared to the alloy WR40.

Dislocation configurations under identical conditions further demonstrate microstructural divergences (**Fig. 6d-f**). It shows irregular interfacial networks with high-density dislocations penetrating the γ' phase in alloys WR20 and WR70, while

larger and geometrically regular networks in alloy WR40. The dislocations generate within the γ matrix during the initial stage of creep. It can move through the γ matrix channels and subsequently pile up at the γ/γ' interfaces, forming dislocation networks. This accumulation concentrates a high density of dislocations at these interfaces. The formation of a dense dislocation network at the γ/γ' interfaces hinders the movement of subsequent dislocations within the γ matrix and impedes their shearing into the γ' phase, thereby mitigating creep damage in the alloy. A regular dislocation network possesses higher stability, enabling it to more effectively hinder dislocation motion and enhance the alloy's creep resistance [37-39]. Consequently, it effectively hinders subsequent dislocation motion, resulting in superior creep rupture performance.

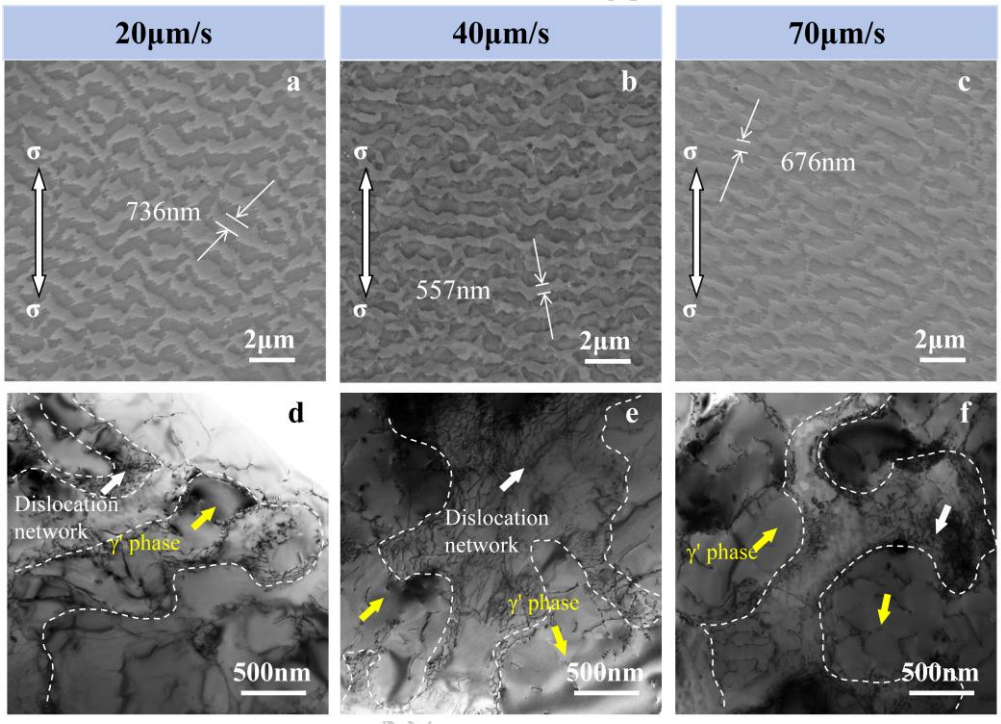

Fig. 6 TEM characterization of post-creep microstructures in Mar-M247LC superalloy. (a-c) withdrawal rate-dependent γ' rafting morphology, (d-f) corresponding interfacial dislocation networks at γ/γ' interfaces.

In addition, it should be noted that the dislocation network in the alloy WR40 demonstrates enhanced density and structural regularity—directly contributing to extended creep life through effective impedance of dislocation propagation. During the creep deformation, dislocations would nucleate in the γ matrix and propagate through γ channels, finally accumulating at γ/γ' interfaces to form dense networks. These interfacial arrays block matrix dislocation motion while preventing shear penetration into the γ' phase, thereby constraining creep damage. Crucially, geometrically ordered networks exhibit superior stability and barrier efficacy.

The dislocation network formation stems from dislocation interactions and lattice misfit (δ) [40]. Per **Eq. (2)** [33]:

$$\delta = \frac{2(a_{\gamma'} - a_{\gamma})}{a_{\gamma'} + a_{\gamma}} \tag{2}$$

where the lattice parameters a_{γ} and $a_{\gamma'}$ depend critically on solute composition. The decomposition of Ta-rich MC carbides releases additional Ta into the surrounding matrix, leading to a localized increase in Ta concentration, raising a_{γ} and consequently an increase in δ [41], promoting denser/more regular networks. As the withdrawal rate increases, the decomposition of the carbides becomes more pronounced. As a result, alloys solidified at higher withdrawal rates exhibit a greater local addition of Ta, thus enhancing the creep resistance**.** However, it should be noted that the increase in Ta content simultaneously increases the γ' phase content in the alloy, which also promotes coarsening of the γ' phase during creep. An excessive amount of the γ' phase can have an adverse effect on the alloy's creep properties [42]. In the alloy WR70, γ' phase coarsening results in wider γ matrix channels. This facilitates rapid dislocation motion

Rare Metal Materials and Engineering

and climb-mediated bypass of γ' precipitates. Consequently, the γ/γ' interface dislocation network density decreases, ultimately diminishing creep resistance.

3.3 Microstructural degradation and creep rupture mechanisms

Microstructural examination of the ruptured specimens after creep rupture testing at 980 °C under 220 MPa is illustrated in **Fig. 7**. The results indicate significant microstructural degradation. The HAADF-STEM image, along with the corresponding EDS mapping, demonstrated that the primary MC carbides underwent decomposition (**Fig. 7a and b**), accompanied by the precipitation of Cr-rich $M_{23}C_6$ carbides. Importantly, continuous γ′ films formed around these degraded primary MC carbides, and microcracks were predominantly localized near carbide clusters (**Fig. 7c-f**). Notably, $M_{23}C_6$ carbides adjacent to microcracks exhibited significantly greater coarsening than those in unaffected regions.

The underlying mechanism for this microstructural degradation and its link to fracture initiation can be described as follows. During creep, the TaC component within primary MC carbides decomposes due to its inferior thermal stability relative to HfC, following the reaction: $MC + \gamma \rightarrow M_{23}C_6 + \gamma'$ [13, 29]. This process consumes solid-solution strengthening elements (e.g., Cr) in the γ matrix, thereby diminishing solid-solution strengthening. Additionally, the formation of continuous γ′ films lowers the resistance to dislocation movement at the γ/γ' interfaces, thus weakening the strengthening effect at the interfaces. As a result, dislocations can more readily destroy the dislocation network under applied stress and cut into the γ' phase, eventually accumulating near the carbides. This leads to stress concentration around the carbides

Rare Metal Materials and Engineering

and promotes crack initiation in these regions. Furthermore, coarsening of $M_{23}C_6$ carbides during creep decreases their pinning effect on dislocations. Consequently, the regions surrounding the decomposed primary MC carbides become microstructurally weak zones, acting as preferred sites for microcrack initiation and propagation.

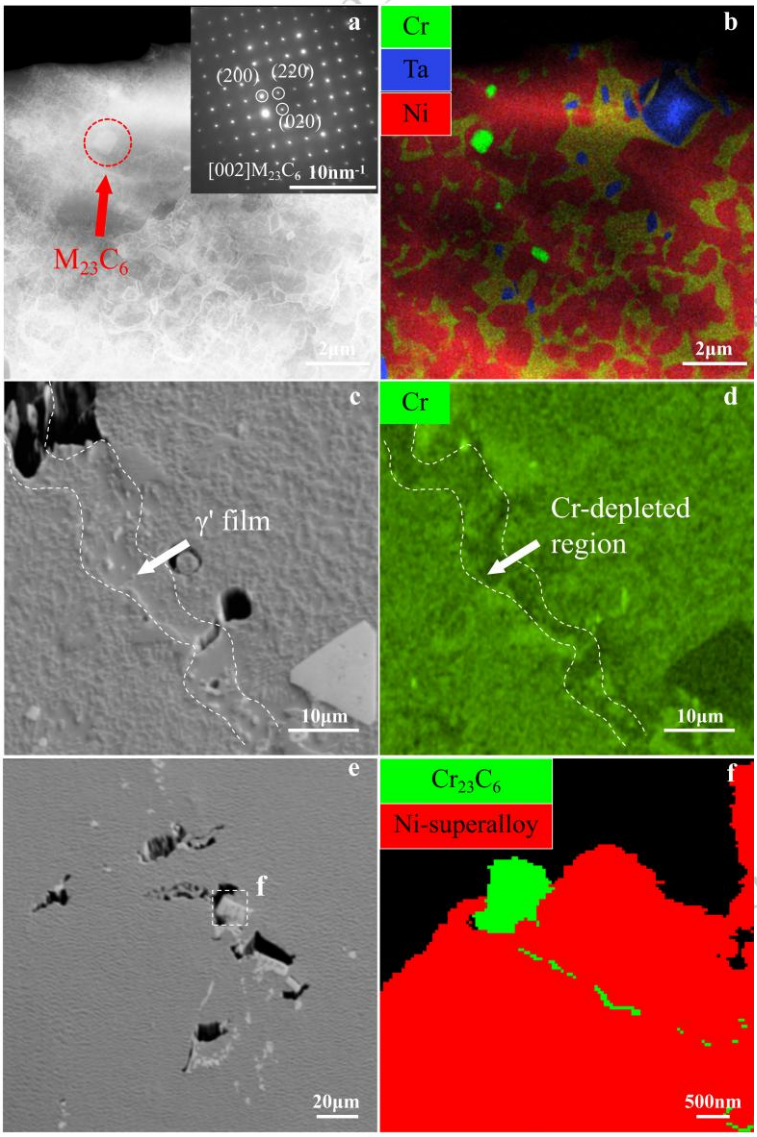

Fig. 7 Microstructural characterization of creep-fractured Mar-M247LC alloy. (a) HAADF-STEM image showing carbides, (b) corresponding EDS elemental map indicating the composition of the carbides in (a), (c) SEM micrographs of Cr-depleted

region, (d) EDS elemental map adjacent to the microcrack shown in (c), (e) SEM micrographs of microcracks, (f) EBSD phase map highlighting $Cr_{23}C_6$ phase.

The fracture morphologies of the three alloys after creep tests are presented in **Fig. 8a-c**. As shown in the inserts, all specimens exhibited pronounced necking and displayed clearly visible dimpled rupture features in the fractography, indicative of a transgranular ductile fracture mechanism under these conditions. EDS analysis of microcracks in the ruptured specimens at different withdrawal rates (**Fig. 8d-f**) revealed enrichment of carbide-forming elements (Ta, W, Hf) around the microcracks. This confirms that crack initiation and propagation occurred preferentially near carbide particles. Therefore, the localized reduction in strength surrounding decomposed primary MC carbides is identified as the predominant mechanism responsible for creep fracture initiation.

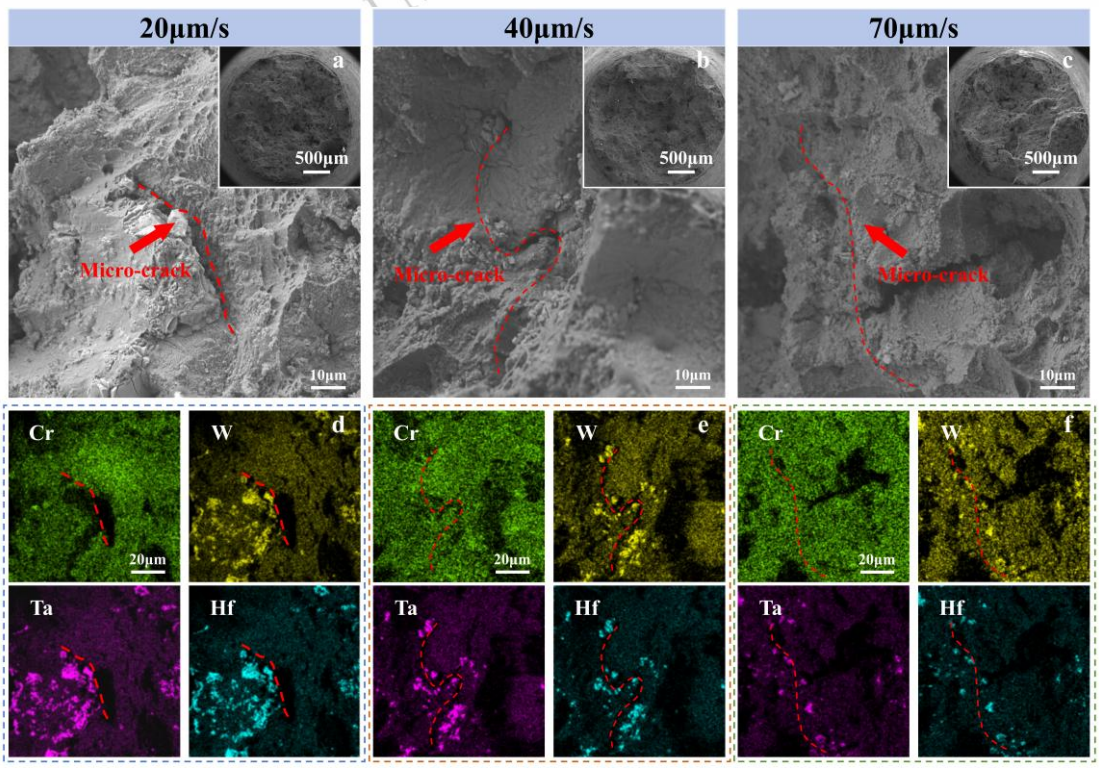

Fig. 8 SEM micrographs showing post-creep rupture fracture morphologies (a-c) and EDS elemental maps of Cr, Ta, W, and Hf adjacent to microcracks (d-f) in Mar-M247LC alloy specimens tested at 980 °C under 220 MPa, processed at different withdrawal rates.

The observed dislocation behavior is integrated into a schematic illustration of the overall creep fracture mechanism for Mar-M247LC at 980 °C and 220 MPa, as shown in **Fig. 9**. Dislocations begin to nucleate within the γ matrix channels and glide under the applied stress, gradually accumulating at the γ/γ′ interfaces. This accumulation results in extensive dislocation pile-ups and the formation of interfacial dislocation networks. During the creep process, the primary carbides in the alloy decompose, leading to the precipitation of $M_{23}C_6$ carbides and the formation of continuous γ′ films. As stress increases, dislocations in the γ matrix disrupt the dislocation networks and penetrate the γ′ precipitates. These dislocations then pile up at the carbides, causing significant stress concentration, which ultimately initiates crack formation. These cracks initiate discontinuously within the specimen interior and propagate perpendicular to the applied stress axis. Ultimately, the coalescence of these microcracks results in predominantly transgranular fracture.

Although variations in the withdrawal rate can influence the microstructure and scale of the Mar-M247LC superalloy, no change in the fracture mechanism was observed. All tested specimens displayed nearly identical fracture mechanisms. Compared to alloys solidified at other rates, the WR40 specimen exhibits elongated rafted γ′ structures and significantly narrower γ matrix channels. This specific

Rare Metal Materials and Engineering

microstructural configuration promotes the development of denser and more regularly dislocated networks at the γ/γ′ interfaces. These enhanced networks act as potent barriers, effectively impeding dislocation glide within the matrix channels. This superior dislocation confinement directly contributes to the extended creep rupture life observed in the WR40 alloy.

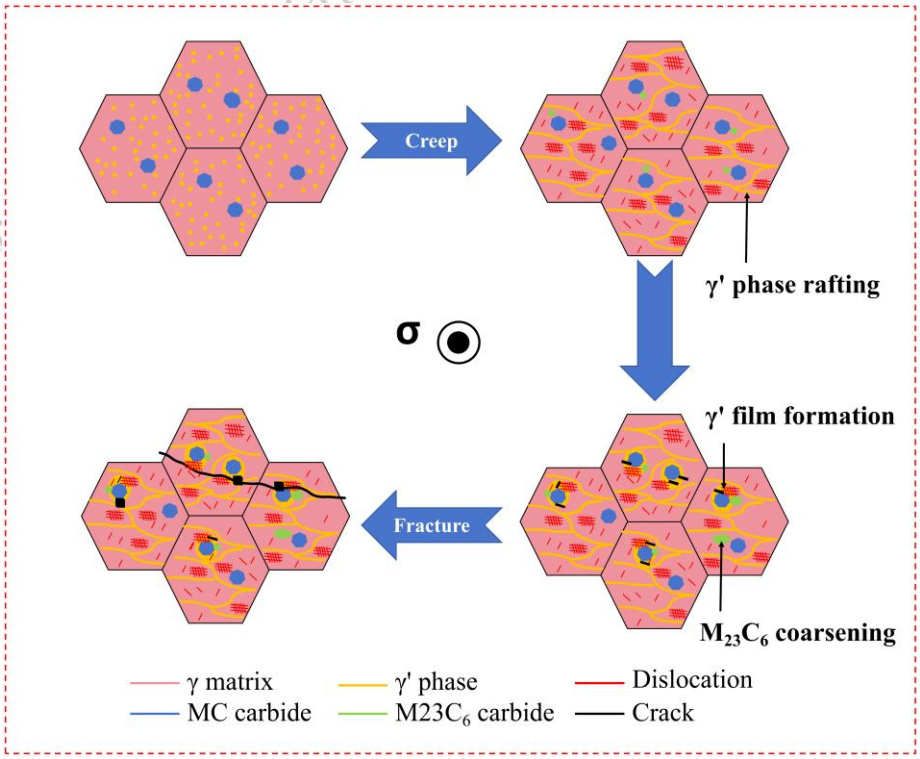

Fig. 9 Schematic diagram depicting the key stages in the creep rupture mechanism of Mar-M247LC alloy at 980 °C/220 MPa, involving dislocation accumulation, microstructural degradation around carbides, weak zone formation, microcrack initiation/propagation, and final transgranular fracture.

4. Conclusions

Based on the comprehensive analysis presented in this study, the following conclusions can be drawn regarding the influence of withdrawal rate on the

microstructure and creep rupture properties of directionally solidified Mar-M247LC nickel-based superalloy:

(1) Increasing the withdrawal rate significantly refines the as-cast dendritic structure and alters the morphology of MC carbide from coarse blocky to fine script-like. Following standard heat treatment, the finer primary carbides exhibit an enhanced propensity for decomposition into minor granular particles. This decomposition releases additional Ta into the matrix, promoting γ' coarsening, with alloy WR70 exhibiting the coarsest γ' morphology.

(2) Alloy WR40, solidified at 40 μm/s, exhibits the longest creep rupture life (96.6 h) under 980 °C/220 MPa, representing increases of 58% and 25% compared to WR70 and WR20, respectively. The superior performance originates from its narrower γ matrix channels and denser dislocation network at the γ/γ' interfaces, which effectively impede dislocation motion. The Ta released from MC carbide decomposition increases the γ/γ' lattice misfit, further facilitating the formation of this beneficial dislocation network.

(3) During creep exposure, the decomposition of primary MC carbides depletes Cr from the surrounding γ-matrix (causing solid-solution weakening) and simultaneously promotes the formation of adjacent continuous γ' films. This synergistic effect critically reduces the localized strength in these regions, creating preferential sites for microcrack nucleation. Once initiated, these microcracks propagate preferentially along paths decorated with coarsened $M_{23}C_6$ carbides, ultimately leading to macroscopic transgranular fracture.

Rare Metal Materials and Engineering

Rare Metal Materials and Engineering
Rare Metal Materials and Engineering
Rare Metal Materials and Engineering

Acknowledgement

This work was supported by State Key Laboratory of Clean and Efficient Turbomachinery Power Equipment (Grant No.DEC8300CG202320387EE280522).

Rare Metal Materials and Engineering

References

1 Gai Y, Zhang R, Yang J et al. Materials Science and Engineering A[J], 2022, 842: 143079https://doi.org/10.1016/j.msea.2022.143079

2 Peng P, Lu L, Liu Z et al. Journal of Alloys and Compounds[J], 2022, 920: 165886https://doi.org/10.1016/j.jallcom.2022.165886

3 Reed R C. The Superalloys: Fundamentals and Applications[M]. Cambridge: Cambridge University Press, 2006https://doi.org/10.1017/CBO9780511541285

4 Ge M, Wang X, Li Y et al. Acta Metallurgica Sinica (English Letters)[J], 2024, 37(11): 1921https://doi.org/10.1007/s40195-024-01753-6

5 Fei X, Sheng N, Sun S et al. Acta Metallurgica Sinica (English Letters)[J], 2024, 37(12): 1995https://doi.org/10.1007/s40195-024-01754-5

6 Peng Z, Tian G, Jiang J et al. Materials Science and Engineering A[J], 2016, 676: 441https://doi.org/10.1016/j.msea.2016.08.101

7 Bhowal P R, Wright E F, Raymond E L. Metallurgical Transactions A[J], 1990, 21(6): 1709https://doi.org/10.1007/BF02672587

8 Baldan R, da Rocha R L P, Tomasiello R B et al. Journal of Materials Engineering and Performance[J], 2013, 22(9): 2574https://doi.org/10.1007/s11665-013-0565-4

9 Yang Y, Wen Z, Pei H et al. Progress in Natural Science: Materials International[J], 2023, 33(3): 343https://doi.org/10.1016/j.pnsc.2023.08.003

10 Wang H, Zhang X, Meng J et al. Journal of Alloys and Compounds[J], 2021, 873: 159794https://doi.org/10.1016/j.jallcom.2021.159794

11 Mirak A, Fathi M. Materials Characterization[J], 2022, 194: 112449https://doi.org/10.1016/j.matchar.2022.112449

12 Ai C, Zhou J, Li S et al. Journal of Alloys and Compounds[J], 2016, 660: 159https://doi.org/10.1016/j.jallcom.2015.11.082

13 Zhang H W, Qin X Z, Wu Y S et al. Materials Science and Engineering A[J], 2018, 718: 449https://doi.org/10.1016/j.msea.2018.02.005

14 Wang J, Zhou L, Qin X et al. Materials Science and Engineering A[J], 2012, 553: 14https://doi.org/10.1016/j.msea.2012.05.077

15 Qin X Z, Wang J Q, Cheng S H et al. Materials Science and Engineering A[J], 2023, 881: 145416https://doi.org/10.1016/j.msea.2023.145416

16 Bor H Y, Wei C N, Jeng R R et al. Materials Chemistry and Physics[J], 2008, 109(2-3): 334https://doi.org/10.1016/j.matchemphys.2007.11.041

17 Szczotok A, Rodak K. IOP Conference Series: Materials Science and Engineering[J], 2012, 35: 012006https://doi.org/10.1088/1757-899x/35/1/012006

18 Rakoczy Ł, Grudzień-Rakoczy M, Cygan R et al. The International Journal of Advanced Manufacturing Technology[J], 2023, 130(3-4): 1321https://doi.org/10.1007/s00170-023-12785-0

19 Li W, Zhao X, Xu J et al. Vacuum[J], 2023, 209: 111780https://doi.org/10.1016/j.vacuum.2022.111780

20 Zhao Y X, Yu J Y, Ma D X et al. Rare Metal Materials and Engineering[J], 2025, 54(8): 1934https://doi.org/10.12442/j.issn.1002-185X.20240435

Rare Metal Materials and Engineering

21 Gao Z, Zhang P, Li J et al. Materials Research Letters[J], 2023, 11(12): 1013https://doi.org/10.1080/21663831.2023.2276340
22 Cheng K, Lv S, Xuan W et al. Materials Characterization[J], 2025, 224: 115009https://doi.org/10.1016/j.matchar.2025.115009
23 Liang Z Y, Wang X G, Tan Z H et al. Materials Characterization[J], 2024, 215: 114137https://doi.org/10.1016/j.matchar.2024.114137
24 Guo X, Antonov S, Lu F et al. Materials Science and Engineering A[J], 2020, 770: 138530https://doi.org/10.1016/j.msea.2019.138530
25 Li Q, Zhang H, Cheng Y et al. Journal of Alloys and Compounds[J], 2022, 923: 166390https://doi.org/10.1016/j.jallcom.2022.166390
26 Liu G, Liu L, Ai C et al. Journal of Alloys and Compounds[J], 2011, 509(19): 5866https://doi.org/10.1016/j.jallcom.2011.02.156
27 Kurz W, Fisher D J. Acta Metallurgica[J], 1981, 29(1): 11https://doi.org/https://doi.org/10.1016/0001-6160(81)90082-1
28 Wang X, Huang T, Yang W et al. Vacuum[J], 2021, 183: 109800https://doi.org/10.1016/j.vacuum.2020.109800
29 Li L, Gong X, Wang C et al. Acta Metallurgica Sinica (English Letters)[J], 2020, 34(6): 872https://doi.org/10.1007/s40195-020-01139-4
30 Xia W, Zhao X, Yue L et al. Journal of Alloys and Compounds[J], 2020, 819: 152954https://doi.org/10.1016/j.jallcom.2019.152954
31 MacKay R A, Ebert L J. Metallurgical Transactions A[J], 1985, 16(11): 1969https://doi.org/10.1007/BF02662398
32 Nathal M V, Ebert L J. Metallurgical Transactions A[J], 1985, 16(3): 427https://doi.org/10.1007/BF02814341
33 Chen J, Chen J, Wang Q et al. Acta Materialia[J], 2022, 232: 117938https://doi.org/10.1016/j.actamat.2022.117938
34 Jahangiri M R, Abedini M. Materials & Design[J], 2014, 64: 588https://doi.org/10.1016/j.matdes.2014.08.035
35 Cui L, Yu J, Liu J et al. Materials Science and Engineering A[J], 2018, 710: 309https://doi.org/10.1016/j.msea.2017.11.002
36 Fan H, Long H, Zhao J et al. Materials Science and Engineering A[J], 2025, 921: 147603https://doi.org/10.1016/j.msea.2024.147603
37 Lv X, Zhang J. Journal of Alloys and Compounds[J], 2016, 688: 449https://doi.org/https://doi.org/10.1016/j.jallcom.2016.07.068
38 Wang R, Li J R, Yue X D et al. Rare Metal Materials and Engineering[J], 2025, 54(10): 2445https://doi.org/10.12442/j.issn.1002-185X.20240540
39 Li Y X, Tian N, Zhang P et al. Rare Metal Materials and Engineering[J], 2025, 54(7): 1733https://doi.org/10.12442/j.issn.1002-185X.20240279
40 Zhang J X, Murakumo T, Koizumi Y et al. Metallurgical and Materials Transactions A[J], 2004, 35(6): 1911https://doi.org/10.1007/s11661-004-0100-1
41 Wu J, Jiang X, Wang Y et al. Materials Science and Engineering A[J], 2021, 806: 140829https://doi.org/10.1016/j.msea.2021.140829
42 Murakumo T, Kobayashi T, Koizumi Y et al. Acta Materialia[J], 2004, 52(12): 3737https://doi.org/10.1016/j.actamat.2004.04.028

Rare Metal Materials and Engineering

抽拉速率对定向凝固 Mar-M247LC 合金微观结构及蠕变性能的影响

甘奕胜[a,1]，王海洋[b,c,1*]，钟 宏[a*]，朱嘉锡[a]，李 博[a]，冯振宇[a]，李双明[a]

(a. 西北工业大学 凝固技术全国重点实验室，陕西 西安 710072)

(b. 清洁高效透平动力装备全国重点实验室，四川 德阳 618000)

(c. 东方电气集团东方汽轮机有限公司，四川 德阳 618000)

摘 要：定向凝固镍基高温合金由于消除了与应力方向垂直的横向晶界，具有优异的蠕变性能。考虑到其蠕变性能与初始凝固组织的强关联性，本文重点研究了抽拉速率对 Mar-M247LC 定向凝固镍基高温合金组织和持久性能的影响。结果表明：随着定向凝固试样抽拉速率的提高，一次枝晶间距逐渐减小（从 479 μm 降至 322 μm），γ'相平均尺寸减小（枝晶间区域从 460 nm 降至 345 nm，枝晶干区域从 298 nm 降至 203 nm）。此外，碳化物形态由块状转变为汉字状。热处理后试样中形成规则的立方状 γ'相，且热处理后试样中的 γ'相含量较定向凝固试样有显著增加。在抽拉速率为 40 μm/s 条件下凝固的合金会形成细长状 γ'筏形组织、狭窄的基体通道及规则的位错网络，这些因素协同作用使蠕变断裂寿命延长至 96.6 小时。断口分析确认其为穿晶韧性断裂，裂纹萌生于分解的 MC 碳化物处。

关键词：定向凝固镍基高温合金；抽拉速率；微观组织；蠕变寿命

Rare Metal Materials and Engineering